



Engineering the Surface Morphology of Inkjet Printed Ag by Controlling Solvent Evaporation during Plasma Conversion of AgNO₃ Inks

| | |
|-------------------------------|--|
| Journal: | <i>Journal of Materials Chemistry C</i> |
| Manuscript ID | TC-ART-12-2021-006174.R1 |
| Article Type: | Paper |
| Date Submitted by the Author: | 25-Feb-2022 |
| Complete List of Authors: | Sui, Yongkun; Sandia National Laboratories, Hess-Dunning, Allison; Case Western Reserve University, Biomedical Engineering; Louis Stokes VA Medical Center, Advanced Platform Technology Center Radwan, Aziz; Case Western Reserve University, Electrical, Computer, and Systems Engineering Sankaran, R. Mohan; University of Illinois at Urbana-Champaign, Nuclear, Plasma & Radiological Engineering Zorman, Christian; Case Western Reserve University, Electrical, Computer, and Systems Engineering |
| | |

ARTICLE

Engineering the Surface Morphology of Inkjet Printed Ag by Controlling Solvent Evaporation during Plasma Conversion of AgNO₃ Inks

Received 00th January 20xx,
Accepted 00th January 20xx

DOI: 10.1039/x0xx00000x

Yongkun Sui,^{*a} Allison Hess-Dunning^{abc}, Aziz N. Radwan^a, R. Mohan Sankaran^d and Christian A. Zorman^{*a}

In this paper, we show that the surface morphology of silver (Ag) structures prepared by plasma conversion of particle-free inks can be controlled by the solvent because of evaporation effects. A series of three ethylene-glycol-based solvents were used to systematically vary the vapor pressure of the ink. Following inkjet printing, films were converted by exposure to a low-pressure, low-temperature radio-frequency (RF) plasma. Scanning electron microscopy (SEM) and profilometry of the Ag films showed that the surface roughness and porosity depend on the vapor pressure of the ink solvent, with each increasing with decreasing vapor pressure. As a result of changes to the porosity, electrical resistivity increased as the solvent vapor pressure decreased. To demonstrate the utility of a metal printing technique for rough and porous films, we fabricated Ag-based hydrogen peroxide (H₂O₂) sensors using inks comprised of the three ethylene-glycol-based solvents. The sensitivity of these sensors was found to be related to the surface roughness and porosity, which in turn, was related to the vapor pressure of the solvent.

Introduction

Printed sensors and electronics are now ubiquitous in healthcare, consumer goods, environmental monitoring and other economically important areas because of their low cost, disposability, reduced materials wastage, and ease of manufacture.¹⁻⁶ For electrochemical sensor applications, printed metal electrodes made from silver (Ag) and gold (Au) are commonly used due to their electrical conductivity, mechanical stability, and tunable surface chemistry.^{7, 8} To broaden the range of detectable chemical or biochemical analytes, efforts have been aimed at functionalizing the electrodes with oxides,⁹ carbon materials,¹⁰ polymers,¹¹ and biomolecules,¹² as well as expanding the number of printable inks to include metals such as platinum (Pt),¹³ palladium (Pd),¹⁴ and bismuth (Bi).¹⁵ The

deposition of the electrodes and functionalization materials can be performed by various additive manufacturing (AM) techniques that enable rapid prototyping and sustainable manufacturing such as direct-ink-writing (DIW),¹⁶ inkjet printing (IJP),¹⁷ screen printing,¹⁸ and aerosol jet printing (AJP).¹⁹ Among these techniques, IJP is a mature non-contact printing method that has been widely used in large-scale manufacturing.²⁰ Roll-to-roll processes that integrate IJP and inline sintering have demonstrated both high reliability and throughput in the production of printed electronics,²¹ solar cells,²² and smart windows.²³

The performance of printed sensors is highly dependent on the effective surface area of the sensing electrode.²⁴ To enhance the sensitivity of metal-based sensors, researchers have explored different approaches to make porous structures with enhanced surface area,²⁵ including de-alloying,^{24, 26} electrochemical deposition,^{27, 28} template deposition,^{29, 30} self-assembly,^{31, 32} and sputtering.^{33, 34} These methods have been applied to sensors,²⁴ as well as other surface-sensitive devices such as fuel cells,³¹ solar cells,³⁵ and batteries,³⁶ yielding devices that significantly outperform those fabricated using fully dense metals. For IJP, the most common metal inks use metal nanoparticles <100 nm in diameter encapsulated in organic stabilizers.³⁷ The nanoparticle inks will produce porous structures after printing, however, the porosity will significantly decrease after a thermal ink curing step, which is required to improve conductivity by remove the organic stabilizers and sinter the particles. Unfortunately, the porosity can only be controlled within a small range; in the case of Ag nanoparticle ink, the porosity was only increased by 8.5% after the curing temperature was decreased from 165°C to

^a Electrical, Computer, and Systems Engineering, Case Western Reserve University, OH, USA

^b Biomedical Engineering, Case Western Reserve University, OH, USA

^c Advanced Platform Technology Center, Louis Stokes Cleveland Department of Veterans Affairs Medical Center, Cleveland, OH, USA

^d Nuclear, Plasma, and Radiological Engineering, University of Illinois at Urbana-Champaign, IL, USA

ysui@sandia.gov; caz@case.edu

† Electronic Supplementary Information (ESI) available: [The supporting information comprises the data related to the characterization of the printed silver (Ag) and plasma system. Fig. S1 contains the X-ray diffraction (XRD) measurement of the printed Ag. Fig. S2 contains higher magnification cross-sectional SEM images of Ag(EG), Ag(diEG), and Ag(triEG). Fig. S3 contains atomic force microscopy (AFM) topology of the printed Ag. Fig. S4 contains the temperature measurement of the plasma chamber as a function of plasma treatment time. Fig. S5 contains the evaporation rate measurement of different solvents in the plasma system. See DOI: 10.1039/x0xx00000x

125°C, which is the minimal temperature to remove the organic ink additives.³⁸

Plasma technology used in conjunction with various printing and spraying processes has enriched the AM toolbox by enabling the synthesis of new materials (*i.e.* non-noble metals, ceramics, etc.) and surface processes (*i.e.* adhesion, chemical functionalization, low-temperature sintering, etc.).^{39–43} While there have been some reports of plasma-assisted printing, the primary focus has been on the chemistry associated with the precursor component of the ink.^{44–47} The importance and possible influence of the ink solvent on material properties has thus far been neglected. In general, the solvent plays a key role during printing, as it affects ink jettability and surface wettability.⁴⁸ Proper selection of ink solvent can also suppress the coffee ring effect by initiating Marangoni flow.⁴⁹ However, ink solvents are usually selected based on their volatility and are assumed to be removed during deposition, and thus are not expected to influence the conversion, chemically or physically. Nonetheless, low vapor pressure solvents that are sometimes used because of their higher viscosity for printing may remain for longer times, even during plasma exposure, thereby influencing the formation of the metallized structure. Therefore, the effect of the solvent on printed metal film fabrication merits further study.

In this paper, we show that the solvent plays a critical role in determining the morphology of Ag films produced by plasma conversion of particle-free inks, and in particular, affects the film surface roughness and porosity. The work builds upon a previous study in which we presented a method to fabricate a hydrogen peroxide sensor by a similar plasma-based printing process.⁵⁰ Our approach involves inkjet printing solutions of silver nitrate (AgNO₃) and an ethylene glycol (EG)-based solvent, followed by exposure to a low-pressure, low-temperature plasma. The EG solvents collectively have relatively low vapor pressures and as a result, the evaporation rate in vacuum is on a comparable time scale as the conversion process. To more systematically test this idea, we utilized a series of EG-based solvents, ethylene glycol (EG), di-ethylene glycol (diEG), and tri-ethylene glycol (triEG), which possess decreasing vapor pressures. Following printing and conversion, the microstructural properties of the Ag structures were assessed by cross-sectional scanning electron microscopy (SEM) and profilometry. With decreasing solvent vapor pressure, thicker and more porous Ag films were obtained, and the surface roughness increased. The electrical resistivities concomitantly decreased with solvent vapor pressure, as the degree of porosity in the films increased. To demonstrate the utility of the porous metal films, we fabricated hydrogen peroxide (H₂O₂) sensors using inks made from the EG-based solvents. We found that the sensitivity increases with decreasing solvent vapor pressure as a result of increasing porosity and surface roughness.

Results and discussion

A diagram of the IJP and plasma conversion process is shown in Fig. 1a. Particle-free inks containing a metal salt precursor, AgNO₃, and an ethylene glycol-based solvent were deposited onto a substrate (*e.g.* polymers, silicon wafers, or glass slides). The as-printed ink was immediately transferred to a vacuum chamber and exposed to a capacitively-coupled, radio-frequency (RF)-powered Ar plasma. Details of this technique to produce printed metal structures can be found in previous publications.^{44, 51} In addition to AgNO₃ the ethylene

glycol-based solvent, the ink contained deionized water. Deionized water aids in achieving the viscosity and surface tension required for proper droplet formation during IJP and increases the solubility of AgNO₃ in the ink. In previous studies, we used EG; here we expanded to diEG, and triEG in order to systematically change the vapor pressure of the ink. Overall, the vapor pressures of EG, diEG, and triEG at ~25°C are 0.089 mm Hg, 0.006 mm Hg, and 0.001 mm Hg, respectively. We hypothesized that varying the vapor pressure of the solvent will change the fraction of time that the printed film remains “liquid-like” during plasma conversion, as illustrated in Fig. 1b. When the film is “liquid-like”, the film components will be solvated, such as AgNO₃ existing as Ag⁺ and NO₃⁻, and be able to diffuse through the film. In addition, plasma interactions with a liquid may lead to unique species such as solvated electrons, hydrogen radicals, and hydroxide radicals.^{52, 53} While we cannot separate these different effects, any one of them or a combination of them may lead to changes in the film such as the depth of conversion, surface roughness, and porosity.

Figure 2 shows SEM images and corresponding energy-dispersive X-ray spectroscopy (EDX) results for cross-sectioned, ~4 μm-thick films produced by plasma conversion of EG-, diEG-, and triEG-based inks. Hereafter, we refer to these samples simply as Ag(EG), Ag(diEG), and Ag(triEG). For the Ag(EG) ink, the plasma converted film exhibits a bi-layer structure consisting of a 1.2 μm thick porous top layer and a 2.8 μm thick dense bottom layer (Fig. 2a). EDX analysis indicates that the top layer consists primarily of Ag (81%), but a small amount of N and O remain (11% and 8%, respectively) (Fig. 2b). X-ray diffraction (XRD) (Fig. S1, Supplementary Information) of the top layer shows peaks associated only with crystalline Ag and no evidence of crystalline AgNO₃ or any other crystalline material. Considering the spatial resolution of EDX,⁵⁴ we believe that the N and O signatures are associated with stray signals from the bottom layer, although it is possible that they are from amorphous N- and O-containing residue in the pores of the top layer. EDX analysis of the bottom layer shows an atomic composition of 50% Ag, 22% N and 28% O, indicative of unconverted AgNO₃. By comparison, Fig. 2c shows that plasma conversion of the Ag(diEG) ink also exhibits a bi-layer structure, but with a slightly thicker top layer (1.6 μm) and a slightly thinner bottom layer (2 μm). EDX analysis again indicates that the top layer is Ag and the bottom layer is AgNO₃ (Fig. 2d). Following this trend, the Ag(triEG) ink is found to produce an even thicker porous top layer (3.1 μm) with no distinct bottom layer (Fig. 2e), which according to EDX analysis is comprised almost entirely of Ag (93%) (Fig. 2f). The low magnification SEM images in Fig. S2 show that the thickness of the Ag(EG), Ag(diEG), and Ag(triEG) structure are relatively consistent within each sample.

Several key differences are revealed by SEM characterization of these films. First, the thickness of the converted layers is found to increase with decreasing ink solvent vapor pressure. Since vapor pressure is related to evaporation rate, the longer the solvent remains in the film during plasma exposure, the longer the film remains in the “liquid-like” state required to sustain conversion-related reactions, in particular AgNO₃ remaining solvated as Ag⁺ and NO₃⁻ and the diffusion of Ag⁺ in the film. We previously showed that electric fields in the film can cause Ag⁺ to electrodiffuse to the film surface and lead to effective conversion of the entire film volume.^{55, 56} We believe such effects are particularly at play for the lowest vapor pressure solvent, triEG, because the film is “liquid-like” for a majority of the

conversion time. Our results also indicate that if the solvent evaporates too quickly, then conversion does not occur deep inside the film, as in the case of EG and diEG. Another reason conversion is enhanced when the solvent remains is the presence of Ag^+ vs. AgNO_3 . We previously showed that the conversion of AgNO_3 to Ag requires gaseous ions to either dissociate or preferentially sputter NO_3^- before

the Ag^+ can be reduced by plasma electrons. The solvation of AgNO_3 and presence of Ag^+ can facilitate reduction directly by plasma electrons. Second, the morphology of the film is linked to the solvent, and in particular the porosity increases with decreasing solvent vapor pressure. The Ag(triEG) ink (Fig. 2f) produces Ag that is more porous than do the Ag(EG) and Ag(diEG) inks (Fig. 2d & 2e).

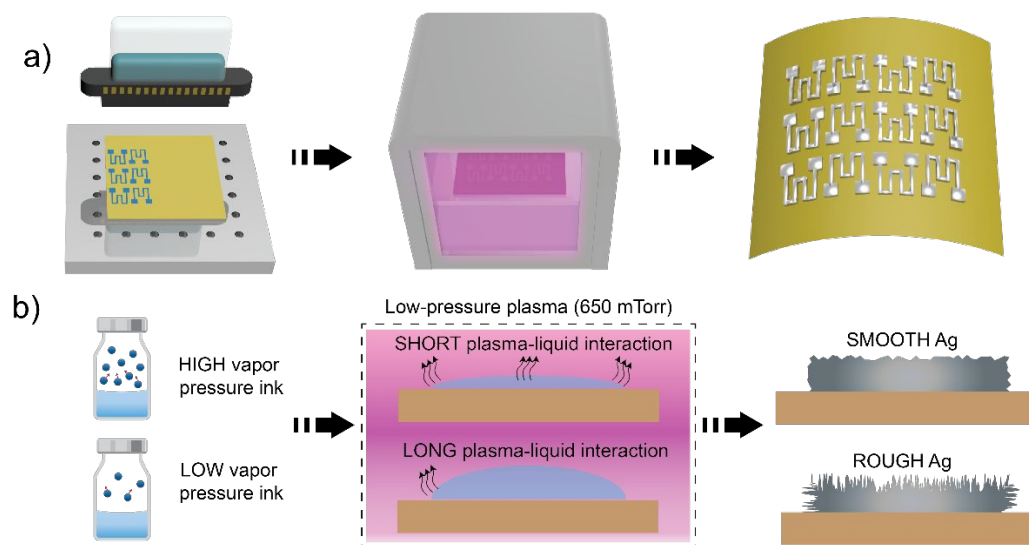


Fig. 1. (a) Process flow diagram for printing Ag from AgNO_3 inks by inkjet printing and low-pressure Ar plasma conversion. (b) Illustration that shows inks comprised of solvents of different vapor pressures yield printed structures with different microstructures.

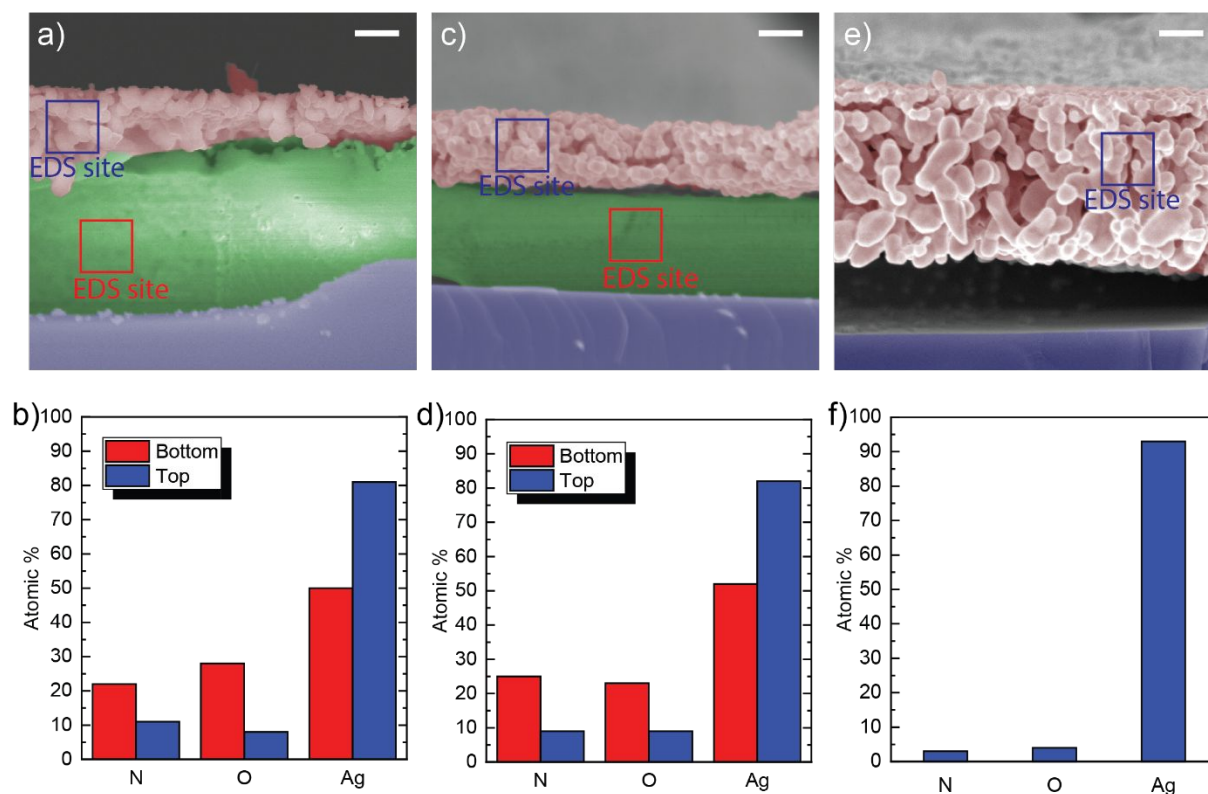


Fig. 2. Cross-sectional SEM images of printed Ag using (a) EG, (c) diEG, and (e) triEG as the ink solvent; EDX elemental composition of printed Ag using (b) EG, (d) diEG, and (f) triEG as the ink solvent. The scale bars in the SEM images represent 1 μm .

ARTICLE

The surface morphology of plasma-converted Ag structures printed from different EG-based inks was initially characterized by optical profilometry. As a control, we also characterized a sputter-deposited Ag film. Optical profilometry was performed over an area of $530 \mu\text{m} \times 710 \mu\text{m}$ and the roughness was assessed. The results in Figs. 3a-d show that all films prepared from EG-based inks are rougher than the sputtered film, and the roughness increases with decreasing solvent vapor pressure. A more quantitative analysis was carried out by creating a histogram of the heights measured by profilometry and calculating the cumulative height distribution as shown in Figs. 3e-h. The analysis indicates that in contrast to the sputter-deposited Ag which exhibits a narrow histogram, the structures printed from EG-based inks show a much broader histogram, ranging from $2.0 \mu\text{m}$ to $2.5 \mu\text{m}$ to $4.2 \mu\text{m}$ as the solvent vapor pressure decreases. All the histograms can be fit to a Gaussian profile, implying that the surfaces are isotropic and the formation of the Ag films is through a cumulative process.⁵⁷ In particular, plasma conversion was performed at a background pressure that suppresses plasma sputtering and etching; the isotropicity of the Ag surface

proves that roughness is not caused by plasma etching which is known to be anisotropic.⁵⁸ The cumulative height distribution curves for Ag(EG), Ag(diEG), Ag(triEG) exhibit progressively steeper slopes for the Ag(triEG) ink, the maximum peaks and valleys are approximately $\pm 4 \mu\text{m}$. The surface morphology of the same films was also characterized by AFM over a smaller area of $40 \mu\text{m} \times 40 \mu\text{m}$ (Fig. S3, Supplementary Information), and revealed similar trends in roughness. The rougher surfaces of the printed structures as compared to sputtered Ag are likely due to the complicated diffusion, nucleation, growth, and agglomeration processes in the printed films. For inks comprised of low vapor pressure solvents, Ag^+ has more time to diffuse, and Ag nuclei have more time to grow and aggregate. It is well known that Ostwald ripening, in which smaller particles are lost because of agglomeration with larger particles, leads to broader particle size distributions. In addition, large Ag particles have melting temperatures close to bulk Ag ($\sim 900^\circ\text{C}$),⁵ and may not be sintered by the plasma, which results in a substrate temperature less than 150°C (Fig. S4, Supplementary Information).

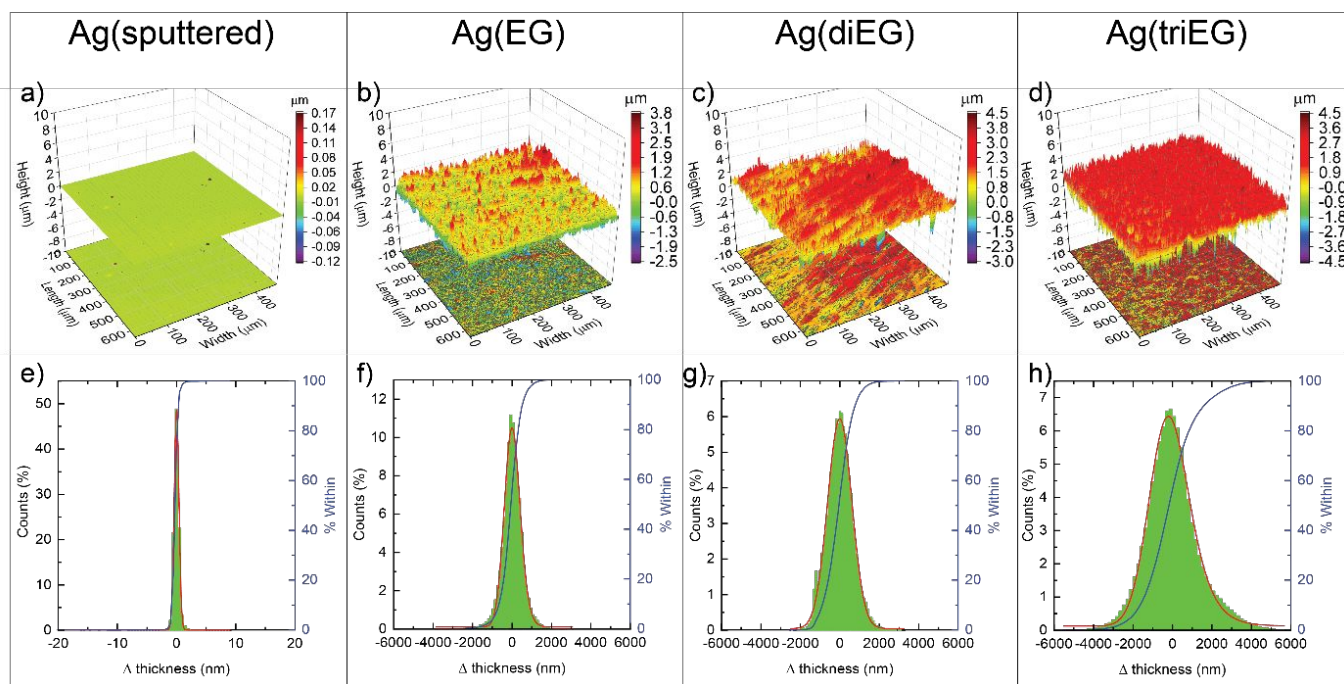


Fig. 3. Optical profile of (a) sputtered Ag, (b) Ag(EG), (c) Ag(diEG), and (d) Ag(triEG); roughness histogram extracted from optical profile for (e) sputtered Ag, (f) Ag(EG), (g) Ag(diEG), and (h) Ag(triEG). The imaging area was $530 \mu\text{m} \times 710 \mu\text{m}$.

The large porosity and surface roughness of the Ag structures printed using EG-based inks lend themselves to surface-sensitive applications such as catalysis and chemical sensing. However, for sensor applications, in particular those that utilize electrochemical transduction, the conductivity of the sensing electrode is also an

important material property because highly conductive materials have high electron transfer rates which, in turn, contributes to high sensitivities.⁵⁹ To assess electrical conductivity, the sheet resistance was measured using the 4-point probe method as shown in Figs. 4a and b. For all ink formulations, the sheet resistance was found to

decrease with increasing plasma exposure time, converging to a minimum value at ~20 min. The sheet resistance of sputter-deposited and bulk Ag are also included for comparison. Four-point probe measurements could not be made until the printed structure was completely solidified, which occurred after 5, 10, and 15 min of plasma exposure for Ag(EG), Ag(diEG), and Ag(triEG), respectively. The minimum sheet resistances in order from smallest to largest were: Ag(triEG) < Ag(diEG) < Ag(EG). To account for different conversion layer thicknesses (see the SEMs in Fig. 2), the resistivity of the Ag films was calculated by using the following formula

$$\rho = R_s \cdot t,$$

where ρ is the resistivity, R_s is the sheet resistance, and t is the thickness of the converted layer. In comparison to sheet resistance, the resistivity of fully treated Ag films was found to completely be reversed in order, with Ag(EG) < Ag(diEG) < Ag(triEG) (Fig. 4d). The resistivity of sputter-deposited and bulk Ag are also included for comparison. The intrinsic resistivity depends on the film morphology, and in this case, the Ag(triEG) ink produced the most porous structure. Voids created during solvent evaporation as well as the broad particle size and poor sintering presumably lead to the high resistivity.

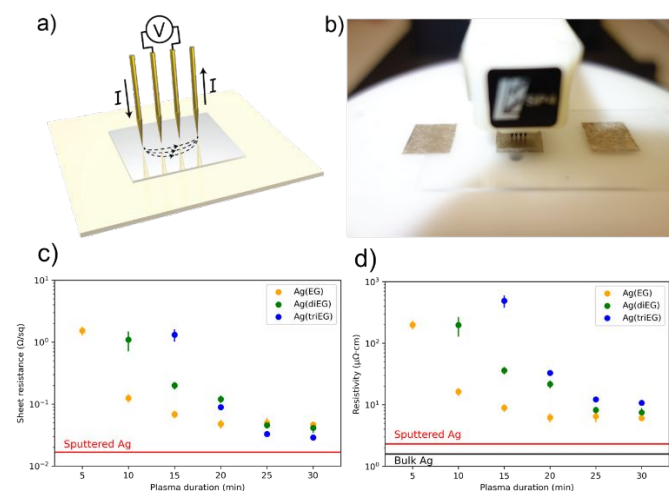


Fig. 4. (a) Illustration of the 4-point probe method; (b) optical image of the 4-point probe setup and printed Ag films under measurement; (c) sheet resistance of sputtered and printed Ag as a function of plasma treatment time [Ag(triEG) data from Ref. 47]; (d) resistivity of sputtered and printed Ag as a function of plasma treatment time [Ag(triEG) data from Ref. 47].

Based on these results, we propose a mechanism for the plasma-based ink activation, as illustrated in Figs. 5a-5d, that can be separated into two components: one when AgNO₃ is ionized in the solvent (Fig. 5a) and one when AgNO₃ has recrystallized due to solvent evaporation (Fig. 5b). After the IJP step, water rapidly evaporates either on the moderately heated substrate holder during printing or during the pump down stage after being loaded into the plasma chamber. In contrast, the EG-based solvent is relatively stable and remains in the printed structure at the onset of plasma exposure. At this point, the printed structure consists of the EG-based solvent and Ag⁺ and NO₃⁻ from the solubilized AgNO₃. The ionic bonds of the AgNO₃ are broken by electrostatic attraction to the polar molecules of the solvent. The resulting ion-dipole interaction is much weaker than

the ionic bonds, resulting in the creation of Ag⁺ within the solvent. The abundant Ag⁺ in solution are readily available for reduction by electrons from the plasma as illustrated in Fig. 5a. It has previously been shown that gas-phase electrons from a plasma can be injected into a solvent to form solvated electrons.⁶⁰ These electrons have a standard reduction potential of -2.77V vs. the standard hydrogen electrode (SHE), which is more than sufficient to reduce Ag⁺ to Ag in solution (reduction potential of 0.80 V vs. SHE).

The interaction between Ag⁺ in solution and solvated electrons from the plasma is largely confined to the near surface region of the printed structure where the electron density is highest and energy loss by the electrons is minimal. The plasma process converts Ag⁺ to Ag in the near surface region, but the Ag⁺ is continually replenished from the bulk (Fig. 5c), transported by a concentration gradient and electric field.^{55, 56, 61} The concentration and size of Ag nuclei continually rises in this region during the plasma conversion process, eventually reaching a level sufficient to trigger nucleation and growth of 3D structures in the near surface region where the plasma electrons have their strongest influence. The as-formed Ag nanoparticles can diffuse through the bulk of the liquid within a couple of minutes,⁶² so they are unlikely to accumulate at the surface. The Ag nanoparticles may aggregate due to their high surface energy, but forming large “raft” structures is unlikely in the presence of solvents because the low temperature plasma is not energetic enough to rapidly remove the solvent molecules surrounding the Ag nanoparticles. Unlike 3D growth on solid surfaces, growth in a liquid suppresses full densification, leading to the porous structure observed in all printed samples. The low vapor pressure solvent permeates the space between the newly forming Ag structures, providing mechanical support for the porous network as well as a source of Ag⁺ for additional nucleation and growth.

The solvent, although relatively stable under vacuum conditions, does evaporate at a steady rate. Argon ion bombardment accelerates this process by moderately heating the film.⁶³ As the solvent evaporates, the cation and anion concentrations increase, and at some point will exceed their solubility limit (Fig. 5b). At this point, the Ag⁺ and NO₃⁻ will begin to react, forming AgNO₃. As the solvent continues to evaporate, the concentration of newly formed AgNO₃ will increase, eventually leading to the formation of crystalline structures in a non-homogeneous manner. Ion bombardment will dissociate crystallites that form near the top surface of the printed structures, and the newly liberated Ag⁺ will be reduced by electrons in the plasma. The effects of ion bombardment will be limited to a relatively small penetration depth that depends on ion energy. For example, our previous studies show that Ar ions of ~800 eV has a penetration depth of ~1.5 μm in AgNO₃.⁵¹ Growth of porous structures from the top and a dense crystalline layer from the bottom continues until all the solvent is evaporated, eventually leading to a bi-layer Ag/AgNO₃ structure (Fig. 5d). The evaporation rates of EG, diEG, and triEG in the low-pressure plasma system were characterized by weighing the solvents before and after plasma treatments. The EG lost 70% of its weight within 5 min and mostly evaporated after 10 min (Fig. S5, Supplementary Information). In contrast, diEG and triEG showed a much smaller evaporation rate under the same conditions and maintained a significant presence up to 15 min and 20 min, respectively (Fig. S5, Supplementary Information). Our picture explains how bilayer films are produced for

EG and diEG, but not for triEG where the solvent remains throughout the plasma conversion and a single layer is formed. In the case of the monoethylene glycol and diethylene glycol inks, the liquid phase reduction ceases after the solvent fully evaporates due to the lack of ionized AgNO_3 . The remaining solidified structure consists of a mixture of Ag particles and crystallized AgNO_3 . There is likely to be a concentration gradient of Ag particles from the top to the bottom of the solidified structure. The top of the structure likely has more Ag particles and less AgNO_3 , because that is where the reduction took place. The residual AgNO_3 within $\sim 1.5 \mu\text{m}$ from the surface of the solidified structure can be reduced to Ag by continued plasma treatment. In the case of the triethylene glycol ink, the liquid phase reduction was prolonged due to the low volatility of the solvent. Most of the AgNO_3 solute was reduced to Ag. The solidified structure formed after the solvent fully evaporates consists of mostly Ag.

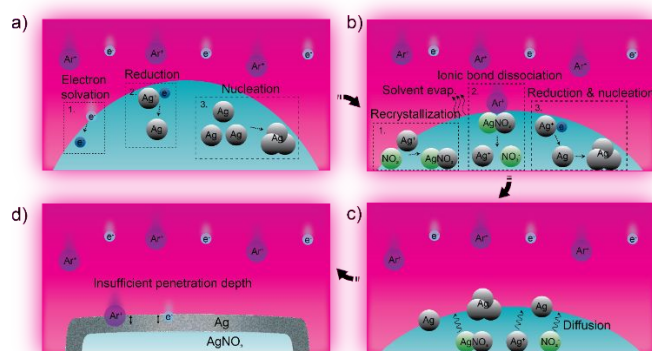


Fig. 5. Proposed mechanism for plasma conversion of EG-based inks containing AgNO_3 consisting of (a) reduction of Ag^+ to Ag by solvated electrons, (b) dissociation of crystallized AgNO_3 to Ag by ionic bond dissociation caused by Ar^+ bombardment, following by reduction of Ag^+ by electrons, (c) transport of precursors (AgNO_3 and Ag^+) to the plasma-liquid interface to continually provide precursor, (d) densified Ag preventing unreacted AgNO_3 from being reacted by plasma.

Electrochemical sensors benefit from electrodes with high porosity and roughness because the large effective surface area facilitates high sensitivity. Meanwhile, high conductivity is also desired because it minimizes Ohmic loss. Unfortunately, porosity and conductivity are generally two opposing properties, therefore a trade-off is usually required. We compared the performance of electrochemical H_2O_2 sensors fabricated from the different EG-based Ag inks with each other and a sputter-deposited Ag control. Each sensor consisted of a sensing electrode, a contact pad, and a narrow metal trace that served as an interconnect. All of these components were comprised of a single Ag layer on a polyimide (PI) substrate. Conductive Ag paste was used to attach wires to the contact pads. The entire sensor except for the sensing electrode was encapsulated by a non-conductive epoxy. A photograph of the sensors is shown in Fig. 6a. Sensor performance was evaluated using the three-electrode electrochemical setup shown schematically in Fig. 6b. In this configuration, the working electrode is the Ag sensor, the counter electrode is a platinum (Pt) mesh, and the reference electrode is a commercial Ag/AgCl electrode. The electrodes were submerged in

1X phosphate buffered saline (PBS) and H_2O_2 of known molarity was periodically added to the PBS to achieve different, known concentrations of H_2O_2 in solution. The current response of the Ag-based sensors resulting from H_2O_2 oxidation to different H_2O_2 concentrations is shown in Fig. 6c. Each step in the current response corresponds to a H_2O_2 concentration increase of 1 mM. As shown by the calibration curves in Fig. 6d, the current response for each sensor exhibits a linear relationship with H_2O_2 concentration. The sensitivity of the Ag electrode printed using Ag(triEG) ink is $-4.69 \mu\text{A}/\text{mM}$, which is the highest among all the sensors. The sensitivity of the Ag electrodes printed using Ag(EG) and Ag(diEG) inks are $-1.73 \mu\text{A}/\text{mM}$ and $-1.07 \mu\text{A}/\text{mM}$, respectively. The sputtered Ag electrode has the lowest sensitivity, which is only $-0.14 \mu\text{A}/\text{mM}$. These results show that sensitivity exhibits a strong dependence on surface roughness, and that the enhanced surface area associated with a rough and porous electrode overcomes the lower electron transfer rate arising from a higher resistivity.

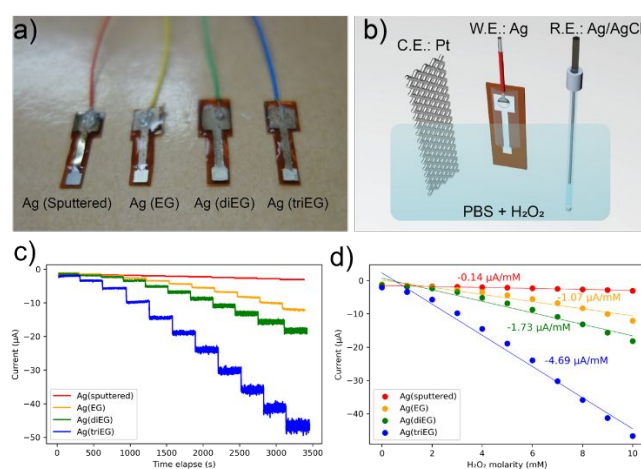


Figure 6. (a) Photograph of the Ag-based H_2O_2 sensors used in this study; (b) schematic diagram of the three-electrode electrochemical sensing setup; (c) current response of the Ag-based H_2O_2 sensors for stepwise increases in H_2O_2 concentration as a function of time [Ag(sputtered) and Ag(triEG) data from Ref. 47]; (d) current vs. H_2O_2 concentration of the Ag-based H_2O_2 sensors [Ag(sputtered) and Ag(triEG) data from Ref. 47].

Conclusions

In summary, a method to engineer the surface roughness and porosity in Ag structures inkjet printed from EG-based, AgNO_3 inks and converted by a low temperature plasma is presented. We found that the roughness and porosity of the plasma-treated structures exhibit a discernable dependence on the vapor pressure of the solvents, with surface roughness and porosity increasing as the vapor pressure of the solvent is decreased. Concurrently, the electrical resistivity increases with decreasing vapor pressure presumably due to increasing porosity in the printed structures. Our findings suggest that the vapor pressure of the solvent determines the length of time over which critical liquid-phase plasma reduction and nucleation steps occur, with low vapor pressure solvents prolonging the conditions of these steps due to their relative stability under vacuum conditions, thus leading to higher

roughness, porosity, and resistivity. The sensitivity of H₂O₂ sensors fabricated by our printing method increased with decreasing solvent vapor pressure suggesting that although the electrical conductivity of the printed structures is compromised due to the porosity, the high surface areas of the rough and porous Ag electrodes compensates for the decrease in electron transfer rate caused by relatively high electrical resistivity. Although this work focused on Ag and a series of EG-based solvents, our findings should be applicable to other metals, such as Au, Cu, and Pt and solvents.

Materials and methods

Ink preparation

AgNO₃ (98% purity, Alfa Aesar), ethylene glycol (Alfa Aesar), diethylene glycol (Alfa Aesar), triethylene glycol (Alfa Aesar), and DI water (Millipore) were used without any further purification. For the EG based Ag ink, 1.5 M AgNO₃ was measured for a 10 ml solution and then dissolved in 9 ml ethylene glycol and 1 ml DI water. For the diEG based Ag ink, 1.5 M AgNO₃ was measured for a 10 ml solution and then dissolved in 9 ml diethylene glycol and 1 ml DI water. For the triEG based Ag ink, 1.5 M AgNO₃ was measured for a 10 ml solution and then dissolved in 8 ml triethylene glycol and 2 ml DI water. DI water was used as a co-solvent to improve the solubility of AgNO₃ in the TriEG ink, and rapidly evaporated during the pump down stage. The inks were mix in a dark environment to minimize reaction under light exposure. The inks were made fresh before printing and used within 1 hour after preparing the solution.

Inkjet printing

Inkjet printing was performed using a Fujifilm Dimatix printer (DMP-3000) equipped with 16 piezoelectric nozzles. The print cartridges used were DMC-11610 with a 10 pl drop size. The as-prepared inks were loaded into the cartridge by a syringe (Fujifilm SYR-003) through a 200 nm filter (Fujifilm FIL-001). Requisite patterns were preprogrammed and the drop sizes, spacing, and nozzle driving waveforms could be tailored using the control program. Printing was performed on cellophane tape (Scotch) for sheet resistance measurement and PI (Kapton) for H₂O₂ sensor fabrication.

Plasma treatment

Plasma treatment was performed in a pure Ar (Purity 99.9999%, Air Gas) environment. The plasma chamber (March PX250) was connected to an external 300 W, 13.56 MHz RF power supply (ENI, ACG-3B-06). The input power, gas pressure and exposure time were controlled directly from the plasma control module. For all experiments, samples were placed on the grounding plate inside the chamber. The chamber was pumped to 60 mTorr and then purged with Ar for 10 min before all experiments to minimize the concentration of foreign gas contaminants. The treatment of the Ag ink was performed at a plasma power of 300 W and an Ar background pressure of 650 mTorr.

Sputter deposition

Sputter deposition of Ag was performed by a Denton DV-502A high vacuum evaporator. The Ag deposition rate is 10.08 Å/s. Ag was deposited through a liquid crystal polymer (LCP) shadow mask that was cut by laser. The deposition started with the shutter closed to

remove oxidized Ag on the target, then the shutter was opened and Ag started to be deposited on the substrate. The depositing time was 5 min, resulting in a Ag film of 300 nm.

Material characterization

The samples for cross-sectional SEM were fabricated by inkjet printing Ag on a pre-scored silicon (Si) wafer. The printed Ag samples were treated in plasma for 30 minutes. The Si wafer and the printed Ag were mechanically snapped into halves to form a cross-section. SEM images were taken by a FEI Nova system. The samples were coated with 5 nm palladium (Pd) to reduce charging effects. Optical profilometry was performed by using a Zygo NewView 7300 optical profilometer. AFM was performed by using an Agilent 5500 scanning probe microscope. The Ag films for sheet resistance measurements were prepared by inkjet printing 1 x 1 cm² squares on cellophane substrates. Three samples were made for each plasma condition to ensure accurate reproducibility. Sheet resistance measurements were performed using a four-point probe station (Lucas Lab 302) and a source meter (Keithley 2400).

Sensor fabrication and test

The sensing electrode of the H₂O₂ sensors is 2 x 2 mm² and the contact pad is 4 x 4 mm². The sensors were made of sputtered or inkjet-printed Ag. The contact pad was connected to electrical wires by using a Ag epoxy (MG Chemicals). The contact pad and the interconnect was covered by a non-conductive epoxy (Devcon). H₂O₂ detection with Ag electrodes was carried out in a three-electrode electrochemical setup consisting of a Pt mesh as the counter electrode, a Ag/AgCl reference electrode, the Ag sensor as the working electrode and a BioLogic SP-300 potentiostat. A beaker was filled with 200 ml 1X PBS (Fisher Scientific), H₂O₂ solution (3% Walgreens) was periodically added to the PBS by using a pipette to increase the concentration of H₂O₂. The solution was constantly stirred by a magnetic stirring bar. To sense changes in H₂O₂ concentration, a -0.7V potential was applied to the Ag electrode versus the Ag/AgCl reference electrode. The current resulting from local H₂O₂ oxidation was measured and recorded at a sampling rate of 10 s⁻¹.

Conflicts of interest

The authors declare no competing financial interest.

Acknowledgements

Y. S., R. M. S, and C. A. Z. gratefully acknowledge funding support for this work by the National Science Foundation (NSF) under Grant No. CMMI-1246715. A. E. H-D. gratefully acknowledges funding support from the United States Department of Veterans Affairs Rehabilitation Research and Development Service under Career Development Award # IK2 RX001841. The authors thank the Advanced Platform Technology Center of the Department of Veterans Affairs for access to the Dimatix DMP 3000 inkjet printer.

References

1. J. A. Hondred, Z. T. Johnson and J. C. Claussen, *Journal of Materials Chemistry C*, 2020, **8**, 11376-11388.
2. M. Ha, S. Lim and H. Ko, *Journal of Materials Chemistry B*, 2018, **6**, 4043-4064.
3. K. Fukuda and T. Someya, *Adv. Mater.*, 2017, **29**.
4. N. C. Raut and K. Al-Shamery, *Journal of Materials Chemistry C*, 2018, **6**, 1618-1641.
5. G. Cummins and M. P. Y. Desmulliez, *Circuit World*, 2012, **38**, 193-213.
6. Q. Huang and Y. Zhu, *Advanced Materials Technologies*, 2019, DOI: 10.1002/admt.201800546.
7. F. Terzi, L. Pigani and C. Zanardi, *Current Opinion in Electrochemistry*, 2019, DOI: <https://doi.org/10.1016/j.coelec.2019.05.005>.
8. Y. Sui and C. A. Zorman, *J. Electrochem. Soc.*, 2020, **167**, 037571.
9. A. Romeo, A. Moya, T. S. Leung, G. Gabriel, R. Villa and S. Sánchez, *Applied Materials Today*, 2018, **10**, 133-141.
10. Y. Fang, M. Akbari, J. G. D. Hester, L. Sydanheimo, L. Ukkonen and M. M. Tentzeris, *Sci Rep*, 2017, **7**, 8988.
11. P. Sjöberg, A. Määttänen, U. Vanamo, M. Novell, P. Ihalainen, F. J. Andrade, J. Bobacka and J. Peltonen, *Sensors and Actuators B: Chemical*, 2016, **224**, 325-332.
12. A. Määttänen, U. Vanamo, P. Ihalainen, P. Pulkkinen, H. Tenhu, J. Bobacka and J. Peltonen, *Sensors and Actuators B: Chemical*, 2013, **177**, 153-162.
13. G. Cummins, R. W. Kay, J. Terry, M. P. Y. Desmulliez and A. J. Walton, presented in part at the Electronics Packaging Technology Conference (EPTC), 2011 IEEE 13th, Singapore, Singapore, 2011.
14. Y. Qin, A. U. Alam, M. M. R. Howlader, N.-X. Hu and M. J. Deen, *Advanced Functional Materials*, 2016, **26**, 4923-4933.
15. Y. Sui, Y. Dai, C. C. Liu, R. M. Sankaran and C. A. Zorman, *Advanced Materials Technologies*, 2019, **0**, 1900119.
16. H. A. Loh, A. R. Graves, C. D. Stinespring and K. A. Sierros, *ACS Applied Nano Materials*, 2019, **2**, 4104-4112.
17. A. Moya, G. Gabriel, R. Villa and F. J. del Campo, *Curr Opin Electrochem*, 2017, **3**, 29-39.
18. A. Hayat and J. L. Marty, *Sensors-Basel*, 2014, **14**, 10432-10453.
19. L.-k. Tsui, S.-v. C. Kayser, S. A. Strong and J. M. Lavin, *Ecs J Solid State Sc*, 2021, **10**, 047001.
20. R. Abbel, P. Teunissen, E. Rubingh, T. v. Lammeren, R. Cauchois, M. Everaars, J. Valetton, S. v. d. Geijn and P. Groen, *Translational Materials Research*, 2014, **1**, 015002.
21. J. Perelaer, R. Abbel, S. Wünsch, R. Jani, T. van Lammeren and U. S. Schubert, *Adv. Mater.*, 2012, **24**, 2620-2625.
22. D. Angmo, T. T. Larsen-Olsen, M. Jørgensen, R. R. Søndergaard and F. C. Krebs, *Advanced Energy Materials*, 2013, **3**, 172-175.
23. S. Lin, X. Bai, H. Wang, H. Wang, J. Song, K. Huang, C. Wang, N. Wang, B. Li, M. Lei and H. Wu, *Adv. Mater.*, 2017, **29**, 1703238.
24. E. Detsi, S. Punzhin, P. R. Onck and J. T. M. De Hosson, *J. Mater. Chem.*, 2012, **22**.
25. R. Zhang and H. Olin, *Materials (Basel)*, 2014, **7**, 3834-3854.
26. M. Hieda, R. Garcia, M. Dixon, T. Daniel, D. Allara and M. H. W. Chan, *Appl. Phys. Lett.*, 2004, **84**, 628-630.
27. D. van Noort and C.-F. Mandenius, *Biosens. Bioelectron.*, 2000, **15**, 203-209.
28. J. Jia, L. Cao and Z. Wang, *Langmuir*, 2008, **24**, 5932-5936.
29. Y. Li, Y.-Y. Song, C. Yang and X.-H. Xia, *Electrochem. Commun.*, 2007, **9**, 981-988.
30. B. Jose, R. K. Vijayaraghavan, L. Kent, S. O'Toole, J. O'Leary and R. J. Forster, *Electrochem. Commun.*, 2019, **98**, 106-109.
31. S. C. Warren, L. C. Messina, L. S. Slaughter, M. Kamperman, Q. Zhou, S. M. Gruner, F. J. DiSalvo and U. Wiesner, *Science*, 2008, **320**, 1748-1752.
32. R. Zhang, M. Hummelgård and H. Olin, *J. Colloid Interface Sci.*, 2009, **340**, 58-61.
33. Y. Liu, J. Liu, S. Sohn, Y. Li, J. J. Cha and J. Schroers, *Nat Commun*, 2015, **6**, 7043.
34. M. Schwartzkopf, A. Buffet, V. Korstgens, E. Metwalli, K. Schlage, G. Benecke, J. Perlich, M. Rawolle, A. Rothkirch, B. Heidmann, G. Herzog, P. Muller-Buschbaum, R. Rohlsberger, R. Gehrke, N. Stribeck and S. V. Roth, *Nanoscale*, 2013, **5**, 5053-5062.
35. R. Y. Zhang, H. A. Andersson, M. Andersson, B. Andres, H. Edlund, P. Edstrom, S. Edvardsson, S. Forsberg, M. Hummelgard, N. Johansson, K. Karlsson, H. E. Nilsson, M. Norgren, M. Olsen, T. Uesaka, T. Ohlund and H. Olin, *Sci Rep-Uk*, 2013, **3**.
36. S. C. Warren, M. R. Perkins, A. M. Adams, M. Kamperman, A. A. Burns, H. Arora, E. Herz, T. Suteewong, H. Sai, Z. Li, J. Werner, J. Song, U. Werner-Zwanziger, J. W. Zwanziger, M. Gratzel, F. J. DiSalvo and U. Wiesner, *Nat Mater*, 2012, **11**, 460-467.
37. J. G. Korvink, P. J. Smith, D.-Y. Shin, Ohio Library and Information Network and Wiley Online Library (Online service), *Journal*, 2012, xvi, 371 pages.
38. J. Vaithilingam, E. Saleh, L. Körner, R. D. Wildman, R. J. M. Hague, R. K. Leach and C. J. Tuck, *Materials & Design*, 2018, **139**, 81-88.
39. J. Hong, A. B. Murphy, B. Ashford, P. J. Cullen, T. Belmonte and K. Ostrikov, *Reviews of Modern Plasma Physics*, 2020, **4**, 1.
40. S. Dou, L. Tao, R. Wang, S. El Hankari, R. Chen and S. Wang, *Adv. Mater.*, 2018, **30**, 1705850.
41. W. Yang, F. Hermerschmidt, F. Mathies and E. J. W. List-Kratochvil, *Journal of Materials Science: Materials in Electronics*, 2021, **32**, 6312-6322.
42. M. Hengge, K. Livanov, N. Zamoshchik, F. Hermerschmidt and E. J. W. List-Kratochvil, *Flex Print Electron*, 2021, **6**, 015009.
43. F. M. Wolf, J. Perelaer, S. Stumpf, D. Bollen, F. Kriebel and U. S. Schubert, *J. Mater. Res.*, 2013, **28**, 1254-1261.
44. V. Bromberg, S. Y. Ma, F. D. Egitto and T. J. Singler, *Journal of Materials Chemistry C*, 2013, **1**, 6842-6849.
45. C. E. Knapp, J. B. Chemin, S. P. Douglas, D. A. Ondo, J. Guillot, P. Choquet and N. D. Boscher, *Advanced Materials Technologies*, 2018, **3**.
46. Y. Farraj, A. Smooha, A. Kamysny and S. Magdassi, *ACS Appl Mater Interfaces*, 2017, **9**, 8766-8773.
47. I. Genish, A. Irzh, A. Gedanken, A. Anderson, A. Zaban and L. Klein, *Surf. Coat. Technol.*, 2010, **204**, 1347-1352.
48. E. Tekin, P. J. Smith and U. S. Schubert, *Soft Matter*, 2008, **4**.
49. H. Hu and R. G. Larson, *The Journal of Physical Chemistry B*, 2006, **110**, 7090-7094.
50. Y. Sui, A. Hess-Dunning, R. M. Sankaran and C. A. Zorman, *J Microelectromech S*, 2020, **29**, 1026-1031.
51. Y. Sui, S. Ghosh, C. Miller, D. Pappas, R. Mohan Sankaran and C. A. Zorman, *Journal of Vacuum Science & Technology A*, 2018, **36**.
52. Q. Chen, J. Li and Y. Li, *J. Phys. D: Appl. Phys.*, 2015, **48**.
53. P. Rumbach, D. M. Bartels, R. M. Sankaran and D. B. Go, *J. Phys. D: Appl. Phys.*, 2015, **48**, 424001.
54. D. B. Williams and C. B. Carter, *Transmission electron microscopy : a textbook for materials science*, Springer, New York, 2nd edn., 2008.
55. S. Ghosh, E. Ostrowski, R. Yang, D. Debnath, P. X. L. Feng, C. A. Zorman and R. M. Sankaran, *Plasma Chem. Plasma Process.*, 2016, **36**, 295-307.
56. S. Ghosh, R. Yang, M. Kaumeyer, C. A. Zorman, S. J. Rowan, P. X. L. Feng and R. M. Sankaran, *Acs Appl Mater Inter*, 2014, **6**, 3099-3104.

57. B. Bharat, in *Modern Tribology Handbook*, ed. B. Bharat, CRC Press, Boca Raton, FL, 2000, vol. 1, pp. 49-114.
58. G. Nageswaran, L. Jothi and S. Jagannathan, *Non-Thermal Plasma Technology for Polymeric Materials: Applications in Composites, Nanostructured Materials, and Biomedical Fields*, 2019, DOI: 10.1016/B978-0-12-813152-7.00004-4, 95-127.
59. J. Wang, B. M. Tian, M. P. Chatrathi, A. Escarpa and M. Pumera, *Electrophoresis*, 2009, **30**, 3334-3338.
60. S. W. Lee, D. Liang, X. P. A. Gao and R. M. Sankaran, *Adv. Funct. Mater.*, 2011, **21**, 2155-2161.
61. V. S. S. K. Kondeti, U. Gangal, S. Yatom and P. J. Bruggeman, *Journal of Vacuum Science & Technology A*, 2017, **35**.
62. H.-J. Kim, J.-G. Shin, C.-S. Park, D. S. Kum, B. J. Shin, J. Y. Kim, H.-D. Park, M. Choi and H.-S. Tae, *Materials (Basel, Switzerland)*, 2018, **11**, 891.
63. M. A. Lieberman and A. J. Lichtenberg, *Principles of Plasma Discharges and Materials Processing, 2nd Edition*, John Wiley & Sons, inc., Hoboken, New Jersey, 2005.